Carbon dioxide photolysis from 150 to 210 nm: Singlet and triplet channel dynamics, UV-spectrum, and isotope effects

Johan A. Schmidt[a,1], Matthew S. Johnson[a,1], and Reinhard Schinke[b]

[a]Department of Chemistry, University of Copenhagen, DK-2100 Copenhagen Ø, Denmark; and [b]Max-Planck-Institut für Dynamik und Selbstorganisation, D-37077 Göttingen, Germany

Edited by Mark H. Thiemens, University of California, San Diego, La Jolla, CA, and approved May 23, 2013 (received for review September 21, 2012)

We present a first principles study of the carbon dioxide (CO_2) photodissociation process in the 150- to 210-nm wavelength range, with emphasis on photolysis below the carbon monoxide + O(^1D) singlet channel threshold at ∼167 nm. The calculations reproduce experimental absorption cross-sections at a resolution of ∼0.5 nm without scaling the intensity. The observed structure in the 150- to 210-nm range is caused by excitation of bending motion supported by the deep wells at bent geometries in the $2^1A'$ and $1^1A''$ potential energy surfaces. Predissociation below the singlet channel threshold occurs via spin-orbit coupling to nearby repulsive triplet states. Carbon monoxide vibrational and rotational state distributions in the singlet channel as well as the triplet channel for excitation at 157 nm satisfactorily reproduce experimental data. The cross-sections of individual CO_2 isotopologues ($^{12}C^{16}O_2$, $^{12}C^{17}O^{16}O$, $^{12}C^{18}O^{16}O$, $^{13}C^{16}O_2$, and $^{13}C^{18}O^{16}O$) are calculated, demonstrating that strong isotopic fractionation will occur as a function of wavelength. The calculations provide accurate, detailed insight into CO_2 photoabsorption and dissociation dynamics, and greatly extend knowledge of the temperature dependence of the cross-section to cover the range from 0 to 400 K that is useful for calculations of propagation of stellar light in planetary atmospheres. The model is also relevant for the interpretation of laboratory experiments on mass-independent isotopic fractionation. Finally, the model shows that the mass-independent fractionation observed in a series of Hg lamp experiments is not a result of hyperfine interactions making predissociation of ^{17}O containing CO_2 more efficient.

mass-independent fractionation | photodissociation dynamics | fine interaction | magnetic isotope effect | Mars

Carbon dioxide (CO_2) is the main component of the atmospheres of Mars, Venus, and the Hadean Earth (1). Its photoabsorption screens solar UV light, determining altitude-dependent photolysis rates, and its concentrations and infrared absorptions make it a powerful greenhouse gas. CO_2 photodissociation is the basis of these atmospheres' photochemistry and is the primary source of carbon monoxide (CO) and O_2. Although the initially high concentration of CO_2 during Earth's Hadean era decreased as carbonate rocks accumulated, CO_2 continued to be a prominent atmospheric gas, enhancing surface temperature and attenuating UV light, with a partial pressure >10 mbar in the Archean (2) and >1 mbar in the Proterozoic (3). Its influence on the radiative properties and chemical composition of Earth's atmosphere has continued to the present day; one example is that CO_2 photolysis is the main source of mesospheric CO (4). Variations in the abundances of naturally occurring stable isotopes, including reaction mechanisms exhibiting mass-independent fractionation, are central to efforts to interpret environmental records ranging from sedimentary rocks to oceanic carbonates to glacial ice (5). Thus, CO_2 photolysis is both directly and indirectly linked to isotopic variations found in the environment.

The UV absorption band of CO_2 ($120\ \text{nm} < \lambda < 210\ \text{nm}$) consists of two broad, strongly overlapping bands peaking around 145 nm and 133 nm, respectively (6). Both exhibit pronounced vibrational structures; those overlaid on the first band are complex, whereas those on the second are more regular. The triplet, $CO(^1\Sigma^+) + O(^3P)$, and singlet, $CO(^1\Sigma^+) + O(^1D)$, dissociation channels open at 227.5 nm and 167.2 nm, respectively. Because of the very small actinic flux below $\lambda < 167$ nm, atmospheric photolysis of CO_2 occurs almost exclusively via the triplet channel except at very high altitudes.

The electronic structure of CO_2 has been the subject of several theoretical studies (7–9). The first quantum dynamics analysis of the UV photoabsorption of CO_2 was provided only recently by Grebenshchikov (10). This work determined 3D potential energy surfaces (PESs) of six singlet states and calculated the absorption cross-section starting near the singlet channel threshold. In contrast, in the present study, we focus on the wavelengths longer than 167 nm, which are important for most atmospheric applications.

CO_2 is a linear molecule with 16 valence electrons, properties common to two other key terrestrial trace gases: nitrous oxide (N_2O) and carbonyl sulfide (OCS)(6). We have recently completed first principle computations of the UV absorption spectra of these two molecules using accurate PESs, the transition dipole moment (TDM) functions coupling them with the ground state, and the quantum mechanical wave packet methodology (11–16). Our calculations do an excellent job of reproducing available experimental data, including the OCS isotopologue absorption spectra (17, 18) and the temperature- and isotopologue-dependent N_2O cross-sections (14, 19).

The wave packet methodology extracts a wealth of information from the potential energy and transition dipole surfaces, including vibrational frequencies; temperature- and isotopologue-dependent absorption spectra; and detailed descriptions of the photodissociation dynamics, including product quantum state, and velocity and angular distributions (20). In practice, the method is limited mainly by the quality of the surfaces. Using the method we have built and tested on N_2O and OCS, we are able to present a similar analysis of the CO_2 UV absorption and dissociation from the onset of the UV spectrum (>210 nm) to *ca*. 150 nm. Our calculations reproduce a variety of existing experimental data; therefore, we can report reliable absorption cross-sections for a set of isotopologues and for a wide range of temperatures by changing the isotopic masses and/or the populations of vibrational states.

Author contributions: J.A.S., M.S.J., and R.S. designed research; J.A.S. performed research; J.A.S. and R.S. contributed new reagents/analytic tools; J.A.S., M.S.J., and R.S. analyzed data; and J.A.S., M.S.J., and R.S. wrote the paper.

The authors declare no conflict of interest.

This article is a PNAS Direct Submission.

[1]To whom correspondence may be addressed. E-mail: johanalbrechtschmidt@gmail.com or msj@kiku.dk.

This article contains supporting information online at www.pnas.org/lookup/suppl/doi:10.1073/pnas.1213083110/-/DCSupplemental.

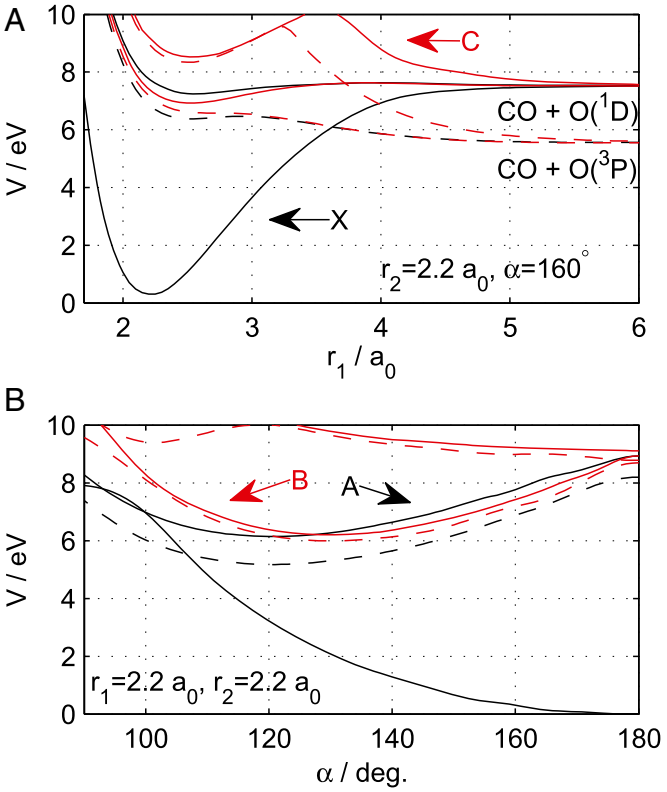

Fig. 1. 1D potential energy curves for the lowest four singlet (full curves) and lowest three triplet (broken curves) electronic states as a function of r_1, one of the two C-O bond lengths (*A*), and as a function of the O-C-O bending angle α (*B*). The A' states (X, A, and a) are shown in black, and the A'' states (B, b, C, and c) are shown in red. In this figure and throughout this article, energy is measured relative to the global minimum of the X state. deg., degree.

Low-Energy Absorption and Dissociation Mechanisms

Six excited electronic states are energetically accessible below ≈ 8.5 eV ($\lambda \approx 150$ nm) in the Franck–Condon (FC) region (Fig. 1): the three singlet states $2^1A'$ (A), $1^1A''$ (B), and $2^1A''$ (C) and the three triplet states $1^3A'$ (a), $1^3A''$ (b), and $2^3A''$ (c) (letters in parentheses indicate abbreviations used below). Fig. 1*A*, which shows 1D cuts along one of the two C-O bonds, r_1, provides an overview of these states and how they connect with the dissociation channels (Table S1); the potential of the ground electronic state $1^1A'$ (X) is also included. Fig. 2*B* shows potential cuts along the O-C-O bending angle α. The potential energies were calculated from first principles using the multiconfiguration reference internally contracted configuration interaction (MRCI) theory (21, 22) including the Davidson correction (MRCI+Q) (*SI Text*). The corresponding potential cuts for OCS and N_2O are qualitatively very similar (12, 13).

The three singlet states A, B, and C have similar energies near linearity ($\alpha \approx 180°$), and they are coupled to one another (10, 23). States A and C form a Renner–Teller pair and are coupled by interaction between nuclear and electronic rotation about the O-C-O axis. The two $^1A''$ states B and C are coupled by nonadiabatic coupling matrix elements (NACMEs) (20). A rigorous theoretical treatment, including the three singlet states (not to mention the 3×3 triplet states), is therefore very challenging. The Renner–Teller and nonadiabatic couplings are largest for linear O-C-O. For total energies below *ca*. 8 eV, however, absorption takes place primarily at angles smaller than $\approx 170°$ (Fig. 1*B*). Therefore, the region close to linearity is not important, and a model in which the couplings between A, B, and C are ignored and the absorption cross-sections are calculated separately for each state is justified.

In our previous studies of photodissociation in N_2O and OCS, which, near linearity, have electronic structures identical to that of CO_2, we used the same model and were able to reproduce the absorption cross-sections very well both at low energies and throughout the first UV band (12, 13).

We have calculated PESs for the ground state X, the three excited singlet states A–C, and the three triplet states a–c using the MRCI+Q method on large 3D grids (*SI Text*, Figs. S1–S3, and Table S1). The calculated energies for the three fundamental vibrations in X$[(0,1^1,0),(1,0,0),$ and $(0,0,1)]$ deviate from the experimental data by 1% (Table S2), which gives an indication of the quality of the potentials. Our earlier studies of N_2O (13) and OCS (11, 12) found equally good agreement between experimental and theoretical vibrational excitation energies. As an example of an excited state PES, Fig. 2 shows 2D representations of the A state PES, V_A, which is the most important one; the corresponding contour plots for the B state are very similar. V_A has a deep well at bent geometries, whose equilibrium energy is 5.532 eV [i.e., 1.961 eV below the (classical) singlet dissociation channel]. The well leads to substantial trapping of the O and CO products during dissociation, even for energies above the singlet channel threshold, and therefore has a strong effect on the absorption cross-section and on the product state distributions. Although the A and B PESs of OCS and N_2O have similar potential wells, they are not as deep and produce only minor structures in the respective absorption spectra (12, 13).

The TDMs of A, B, and C with the ground electronic state (e.g., μ_A) have been calculated at the MRCI level on small

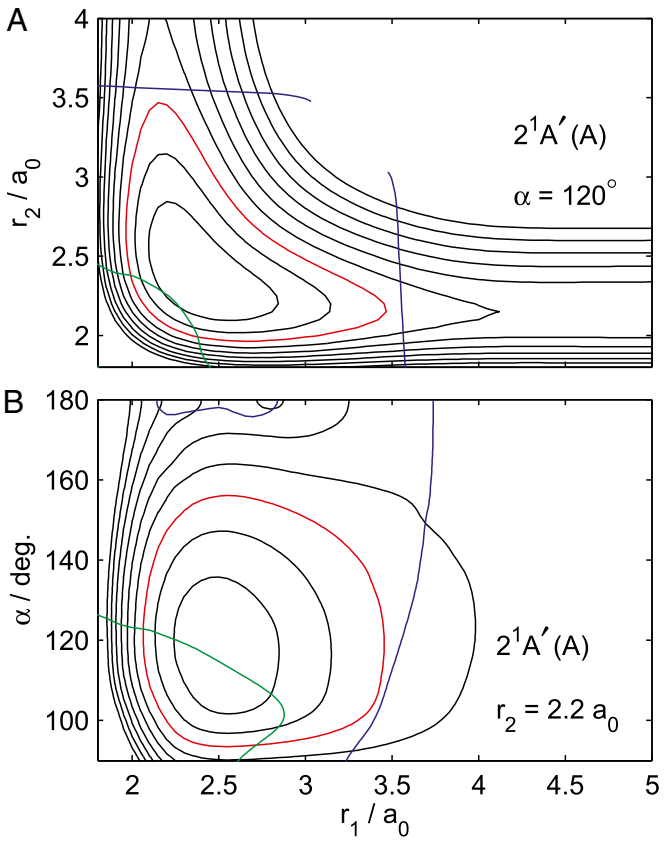

Fig. 2. 2D representations of the A state PES as a function of the two C-O bond lengths r_1 and r_2 (*A*) and as a function of one C-O bond length and the O-C-O bond angle α (*B*). The red contour is at 7 eV, and the green and blue lines mark the seam of intersections with the triplet states b ($1^3A''$) and c ($2^3A''$), respectively. The spacing between the contours is 0.5 eV.

coordinate grids around the FC region (*SI Text*). The transition to the A state is dominant because μ_A is the largest (Fig. S4). It lies in the plane of the molecule and has two components, μ_A^y and μ_A^z. The B state TDM, μ_B, has a single component perpendicular to the molecular plane. The μ_A^z increases rapidly as the molecule bends, whereas μ_A^y and μ_B increase along the asymmetrical stretch coordinate and have similar values. The C state TDM is very small compared with μ_A and μ_B; therefore, excitation of the C state has been neglected in the calculations.

There is an additional complication. The X and A states belong to different irreducible representations in the C_{2v} configuration; therefore, their PESs are allowed to cross along the $r_1 = r_2$ symmetry line [conical intersection (CI)]. This happens around $\alpha \approx 100°$, as seen in Fig. 1*B* and Fig. S1. When $r_1 \neq r_2$, the two states belong to the same irreducible representation (C_s) and the potentials form an avoided crossing. In the vicinity of the CI, states A and X are coupled through a NACME and the manifolds of vibrational states belonging to either A or X are mixed. The low-energy part of the measured absorption spectrum reflects this mixing in the form of irregular subnanometer structures.

Below the singlet channel threshold (≈ 7.75 eV), dissociation from X, A, or B is only possible via coupling to the repulsive triplet state a, b, or c. Spin-orbit (SO) coupling splits each (zero-order) triplet state into three components with $m_s = 0, \pm 1$. The SO coupling elements between the singlet and triplet states have been calculated as described for N_2O (16) (*SI Text*), and the elements involving A and B are shown in Figs. S5 and S6. Most important is the coupling between A on one hand and b_0 and c_0 on the other; the corresponding SO elements exceed 0.01 eV in the vicinity of the intersection seams, which are indicated in Fig. 2*B*.

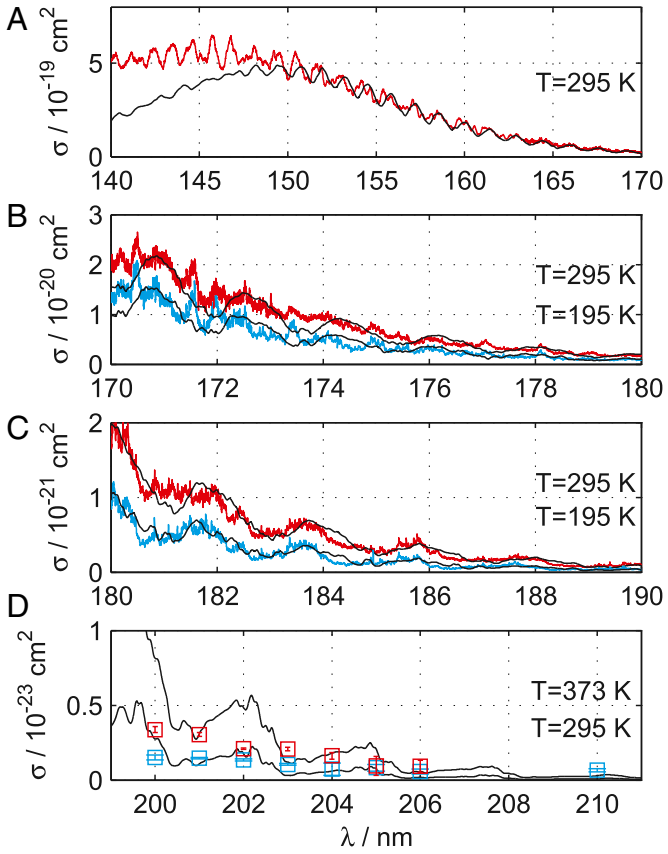

Fig. 3. Comparison of calculated (black lines) and measured (red and blue lines and symbols) absorption cross-sections in different wavelength regions and for several temperatures. The experimental data in *A–C* are from Yoshino and colleagues (24, 25) (www.cfa.harvard.edu/amp/ampdata/co296/co2.html), and the single-wavelength results in *D* are from Karaiskou et al. (26). T, temperature.

Absorption Cross-Section

Temperature-dependent absorption cross-sections were calculated for states A and B separately, using wave packet propagation (*Materials and Methods*). The total cross-section is the sum of σ_A and σ_B. The cross-section for state C was neglected in the analysis because of the very small TDM. Fig. 3 shows the calculated absorption cross-section, shifted by 100 cm^{-1} to lower energies, at different temperatures in comparison to experimental data. Similar shifts were applied in our studies of N_2O (13) and OCS (12), and are necessary due to small inaccuracies in the calculated electronic excitation energies. We emphasize that the intensity of the calculated cross-section was not scaled, as was done for other molecules [e.g., OCS (12) and N_2O (13)]. Fig. 3*A* shows an overview from 140 to 170 nm. The underestimation below 150 nm is due to the neglect of higher electronic states [i.e., the more intense 133-nm band (10)]. Above 150 nm, the agreement with the measured cross-sections is very good even at the longest wavelengths, where the cross-section has fallen by about six orders of magnitude. The temperature dependence is also reproduced. Karaiskou et al.'s data (26), shown in Fig. 3*D*, have orders of magnitude higher resolution, so they can only be used to show trends.

At very long wavelengths, excitation of the B state is dominant, whereas at shorter wavelengths σ_A predominates. The ratio σ_A/σ_B is about 9 at 150 nm; the crossover occurs at around 200 nm. Excitation of vibrationally excited states of X plays a significant role in the studied region. At 170 K, for example, the $\sigma_{(010)}/\sigma_{(000)}$ ratio is ~ 0.1 at 166 nm and ~ 0.2 at 180 nm; at 300 K, these ratios increase to ~ 0.5 and ~ 1, respectively. This behavior is driven by the slope of the transition dipole surfaces (Fig. S4).

The theoretical and experimental cross-sections show undulations whose positions and amplitudes are largely reproduced by the calculation. The spacing is about 650 cm^{-1} at 200 nm and 520 cm^{-1} at 150 nm. The undulations correspond to a clear recurrence of the (0,0,0) autocorrelation function with a period of $\approx$60 fs. As for OCS (12), the structure mainly arises from bending motion in the deep wells of V_A and V_B at bent geometries, above and below the singlet channel threshold.

Superimposed on the undulations, the calculated spectrum, and, to a lesser extent, the measured spectrum exhibit additional structure (Fig. 3 *B–D*) that arises from specific highly excited stretching/bending states of A and B. Moreover, the experimental spectra show details finer than the calculated spectra (Fig. 3*C*). These structures probably represent vibrational states in the dense quasicontinuum of the X state, which is coupled to the A state as described above. Because the X state is not included in the model, the calculated spectrum does not show these fine irregular spectral features.

Full reproduction of the experimental spectrum in the long-wavelength region would require prohibitively high accuracy for all PESs and coupling surfaces. In this work, we focus on reproducing the low-resolution undulations, the general increase with photon energy, and the magnitude of the absorption cross-section. This allows us to calculate cross-sections and fractionation spectra for all isotopologues and for temperatures from 0 to 400 K, with sufficient accuracy to derive reliable loss rates and isotopic fractionation for broadband photolysis in planetary atmospheres (*SI Text*, Datasets S1–S6). However, because of the resolution limit, the results cannot be directly applied to the question of self-shielding.

Product State Distributions for Excitation at 157 nm

A separate model was constructed explicitly considering the SO coupling of the A state to the b_0 and c_0 triplet states (*Materials and Methods*). This model was used to calculate the $O(^3P)/O(^1D)$ branching ratio, as well as the rotational (j) and vibrational (v) distributions of product CO in the singlet and triplet channels for

photodissociation at 157 nm. The calculated $O(^3P)$ yield of 12% agrees reasonably well with the experimental estimate of 6 ± 2 % (27). The singlet channel rotational distribution (Fig. S7) for $v=0$ ($v=1$) shows irregular oscillations from the onset at $j=0$ up to $j \approx 40$ ($j \approx 30$), where the distribution is essentially zero in good agreement with experiments (28). The triplet channel rotational distributions (Fig. S7) are qualitatively similar but extend to much higher values of j. The vibrational distribution of the singlet channel is narrow and peaks at $v=0$. The $CO(v=0)/CO(v=1)$ ratio is 4.15, in excellent agreement with the measured value of 3.7 ± 1.2 (28). The triplet vibrational distribution also peaks at $v=0$ but falls off much more slowly with v, extending to $v=8$. The total kinetic energy distribution constructed from the vibrational-rotational distribution agrees qualitatively with the measurement (29). A more detailed discussion will be published elsewhere.

Isotope Effects

Wavelength-dependent isotopic fractionation constants $\epsilon(\lambda)$ (*Materials and Methods*) for three isotopologues are shown in Fig. 4 *B* and *C*. In Fig. 4*B*, the ε constants are averaged over 0.25 nm, which is sufficiently narrow to show the range of fractionation generated by the undulations. Isotopic substitution alters the vibrational wave functions and energy levels of both the ground and excited states. The isotope shifting brings the undulations in the cross-sections for the heavier isotopologues out of phase with the undulations of the light $^{12}C^{16}O_2$ (Fig. 4*A*), leading to the periodic oscillations. They vary rapidly with wavelength and can range from −500‰ to 500‰ over an interval of just a few nanometers.

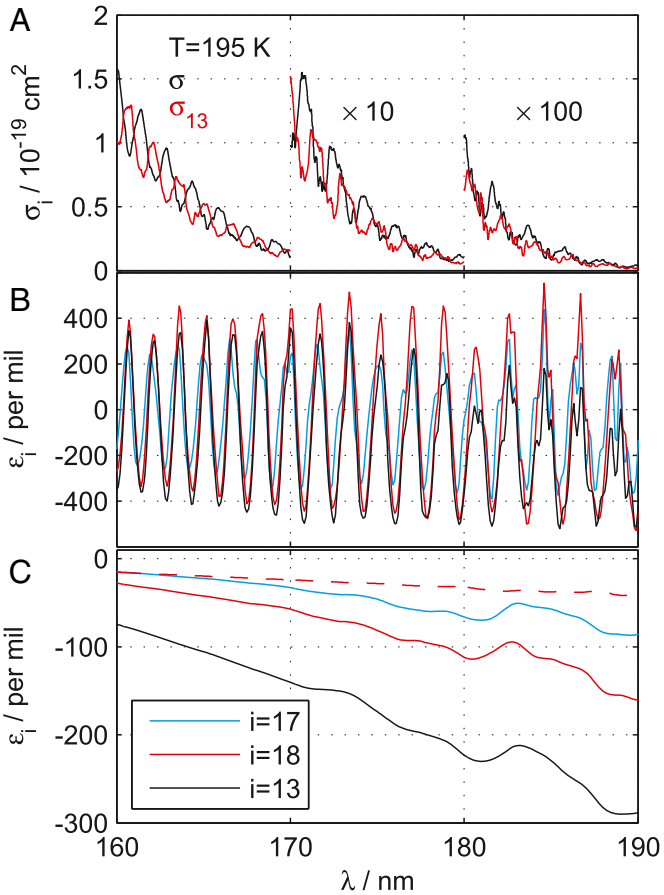

Fig. 4. (*A*) Calculated cross-sections for $^{12}C^{16}O_2$ and $^{13}C^{16}O_2$. (*B* and *C*) Calculated fractionation constants ($\epsilon_i = \sigma_i/\sigma - 1$) as a function of wavelength for different isotopologues of CO_2. Results were averaged over a Gaussian window with FWHMs of 0.25 nm (*B*) and 2.5 nm (*C*). The broken red line in *C* shows ϵ_{18} calculated using the ZPE method (30). per mil, parts per thousand.

Fig. 4*C* shows the fractionation constants averaged over a 2.5-nm window, chosen to illustrate broadband fractionation effects. Photolytic fractionation is increasingly negative with increasing wavelength. At very low photon energies (long wavelengths), absorption takes place mainly into the lower vibrational states, which are localized around the bent minimum of the A and B state PESs. Because the X-state wave functions, localized near linearity, are narrower for the heavier isotopologues, the overlap with the bent vibrational states of A and B becomes smaller with isotopic substitution. This general effect is amplified by the fact that the TDM decreases with the bending angle (i.e., when CO_2 becomes more linear).

We have included a zero point energy (ZPE) method-based prediction of the $^{12}C^{18}O^{16}O$ fractionation in Fig. 4*C*. The magnitude of the fractionation is approximately threefold smaller for the ZPE method compared with the wave packet results (Fig. 4*C*). A similar underprediction by the ZPE method, arising from the slope of the transition dipole surface and changes of the vibrational wave functions with isotopic substitution, is observed for N_2O (14) and OCS (17, 18). The ZPE method is a semiempirical approach, which uses the cross-section for one isotopologue (typically the most abundant) and the ZPEs of the different isotopologues to estimate the cross sections of the remaining (rare) isotopologues. The ZPE method is convenient because the required data (cross-sections and ZPEs) are often readily available. Unfortunately, the method has numerous shortcomings; for example, it does not consider changes to the width of the cross-sections, changes in the vibrational energy levels of the excited state, or changes in the overall magnitude of the cross-sections due to the TDM. The ZPE method was introduced by Yung and Miller (30) to investigate the isotopic fractionation in N_2O photolysis. The ZPE method was later applied to O-isotope fractionation in CO_2 photolysis (31). Our results demonstrate that the ZPE method is not well suited to describe fractionation in CO_2 photolysis.

Fig. 5 shows results from a simulated photolysis experiment using a Gaussian lamp spectral function with the center varied from 160 to 190 nm and a width of 2.5 nm (*Materials and Methods*). The simulation continues to 50% photolysis of the initial $^{12}C^{16}O_2$. There is a significant increase in $\delta^{13}C$ and $\delta^{18}O$ of the remaining CO_2 with λ. The value of $\Delta^{17}O$ has both positive and negative excursions from zero. The average value of $\Delta^{17}O$ from 160 to 190 nm is 0.8‰, which is small considering the large value of $\delta^{18}O$ (58.8‰) and the large extent of reaction, showing that the general trend in fractionation of oxygen isotopes is close to being mass-dependent. The Δ_{47} value shows larger departures from zero. The sign of Δ_{47} depends intricately on λ; the average value in the plotted interval is −1.44‰. Because actinic flux decreases sharply by *ca.* 10^3 between 190 and 180 nm, there is a distinct possibility of producing mass-independent fractionation and a clumped isotope anomaly when CO_2 is photolyzed in planetary atmospheres. These implications will be explored in detail in a forthcoming publication.

In a series of experiments, Bhattacharya and colleagues (32–34) measured the isotopic fractionation caused by CO_2 photolysis. The experiments used a mercury lamp with an emission at 184.9 nm. The widths of the emission were cited to be 10 nm (32) and 2 nm (33). This light is below the singlet channel dissociation threshold at 167 nm, and dissociation can only proceed via coupling to the triplet states. The experiments (32, 33) found that product CO and O_2 are significantly enriched in ^{17}O, although being neither enriched nor depleted in ^{18}O compared with the initial CO_2. This observed mass-independent fractionation was interpreted as evidence of a predissociative mechanism dominated by hyperfine interaction, particularly coupling between singlet and triplet electronic states dependent on both the electronic and nuclear

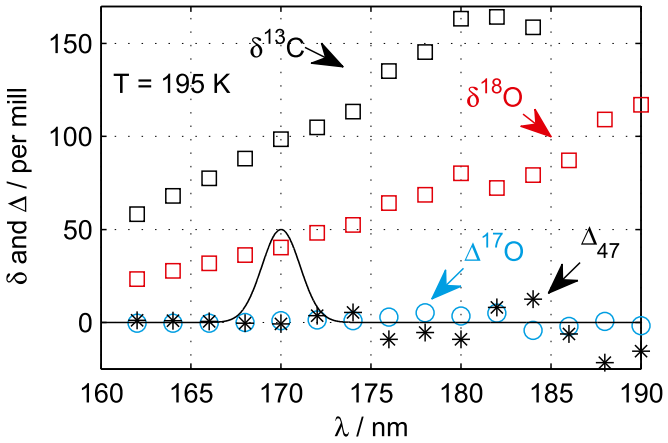

Fig. 5. Simulated $\delta^{13}C$, $\delta^{18}O$, $\Delta^{17}O$, and Δ_{47} of the remaining CO_2 for photolysis using a Gaussian lamp spectrum with a FWHM of 2.5 nm and a moving center at λ. The full black line shows an example of the lamp spectrum at $\lambda = 170$ nm. The photolytic yield was set to 50%.

spin (^{16}O and ^{18}O are spin 0, whereas ^{17}O is spin 5/2). The hypothesis is that that CO_2 containing one or more ^{17}O nuclei predissociates more efficiently (i.e., faster) than other CO_2 isotopologues, which therefore have a higher probability of being quenched radiatively or through collisions. Our results contradict this interpretation because it would require SO-induced predissociation onto the triplet surfaces to be inefficient; otherwise, SO coupling (fine interaction) would completely overshadow any predissociated induced effects sensitive to the nuclear spin (hyperfine interaction). However, in the case of CO_2, the fine interactions are strong (e.g., Figs. S5 and S6) and give rise to fast predissociation on a time scale of several picoseconds. Our assertation, that hyperfine interactions are not causing the observed fractionation pattern, is further supported by the observed photolysis quantum yield of unity at 184.9 nm (35) for CO_2, which leaves no room for a preferential predissociation of ^{17}O-substituted CO_2. The experimental results (32–34) can be explained if the width of the Hg emission is narrower than indicated, with structure on a subnanometer scale. The experimental observations may arise from resonance between the narrowly structured emission lines of the lamp and the isotopologue-dependent fine structure of the CO_2 cross-section. This would also explain the very large variation in the isotopic fractionation with temperature (34), because relatively small differences in temperature lead to significant differences in the population of the rotational states, which can have a large effect on the fine structure of the cross-sections. High-resolution measurements of the isotopologue-specific cross-sections of CO_2 similar to studies performed for SO_2 (36, 37) are needed to fully unravel isotopic fractionation fully on a subnanometer scale.

Materials and Methods

Potential energy energy surfaces for the $1-3^1A'$, $1-3^1A''$, $1-3^3A'$, and $1\ 3^3A''$ electronic states were constructed using the MRCI+Q method (21, 22) and Dunning's aug-cc-pVQZ (38) orbital basis set. Further details are given in *SI Text*.

Absorption cross-sections for different isotopologues of CO_2 were calculated using time-dependent quantum mechanical methodology (20, 39). Wave packets were propagated on the uncoupled A and B excited state PESs, and the cross-sections were obtained by Fourier-transforming the autocorrelation functions. The calculations were performed in terms of the Jacobi coordinates R (distance from one O atom to the center-of-mass of the product CO), r (bond length of the product CO molecule), and γ (angle between R and r). The initial wave packets were defined as the product of a vibrational state of the X state and the modulus of the A or B state TDM. The wave packets were propagated in time using a Chebychev polynomial expansion of the time evolution operator (40). The action of the Hamiltonian on the wave packet was evaluated using the pseudospectral scheme of Le Quéré and Leforestier (41). The Fourier method (42) was used to evaluate the action of the radial kinetic energy operators, whereas the action of the angular kinetic energy operator was evaluated by transforming between a grid representation and a basis set representation consisting of associated Legendre polynomials, $\{Y_l^m\}$, with $m = 0, 1, 2,$ or 3 depending on the initial vibrational state. The lowest nine vibrational states were considered for the calculation of thermal cross-sections. The dynamics calculations were carried out using the Wavepacket program package (43).

All quantum dynamics calculations were performed with a total angular momentum $J = 0$. This is an approximation and does not satisfy the selection rules for dipole excitation. A rigorous treatment with $J \neq 0$ is a formidable computational task, which, if the spectrum does not show rotational resolution, merely leads to some, usually less interesting, broadening. All our calculations for N_2O and OCS used the $J = 0$ approximation, and very good agreement with the measured spectra was achieved. In the present study, rotational effects were approximately accounted for by level-shifting the cross-sections using a linear rigid rotor-guided approach and the selection rule $\Delta J = \pm 1$. This effectively led to a temperature-dependent broadening of the narrow lines. The bands are also broadened by coupling of all singlet states to the repulsive triplet states; however, this effect is overshadowed by the rotational broadening. Nonadiabatic coupling between the A and X states causes mixing of the vibrational states of A with the quasicontinuum of X, which leads to additional strong broadening. This effect was empirically accounted for by averaging the A state cross-sections with a Gaussian with a FWHM of 250 cm^{-1}. Calculated absorption cross-sections for five isotopologues and temperatures from 120 to 395 K are available in *SI Text* (Datasets S1–S6).

When calculating the product state distributions and the singlet/triplet branching ratio, the SO coupling of the A state to the b_0 and c_0 triplet states was explicitly taken into account (i.e., three coupled wave packets were propagated simultaneously). These calculations were performed on a larger grid extending further along R than used in the calculations for the spectra. The methodology used was similar to that described by Schinke et al. (16) for N_2O.

The wavelength-dependent fractionation constants were defined as $\epsilon_i = \sigma_i/\sigma - 1$ ($i = 17, 18,$ and 13), where σ, σ_{17}, σ_{18}, and σ_{13} are the cross-sections for $^{12}C^{16}O_2$, $^{12}C^{17}O^{16}O$, $^{12}C^{18}O^{16}O$, and $^{13}C^{16}O_2$, respectively. The simulation in Fig. 4*C* was carried out as follows: The rate of photolysis for all relevant isotopologues was calculated for different values of λ (the center of the lamp spectrum) as

$$j_i = \int \sigma_i(\lambda') \exp\left[-\alpha(\lambda' - \lambda)^2\right] d\lambda'. \quad [1]$$

The FWHM of the lamp spectrum was set to 2.5 nm. The photolysis yield was 50% [i.e., $[^{12}C^{16}O_2]_t/[^{12}C^{16}O_2]_0 = \exp(-j_{16}t) = 0.5$]. The initial isotopic composition of CO_2 was assumed to be stochastic, and the oxygen and carbon isotope ratios were set to those of Vienna Standard Mean Ocean Water and Vienna Pee Dee Belemnite (i.e., $[^{17}O]/[^{16}O] = 0.03799$ %, $[^{18}O]/[^{16}O] = 0.2005$ %, and $[^{13}C]/[^{12}C] = 1.079$ %). The δ and Δ values were calculated as

$$\delta^{18}O = \frac{R^{18}}{R^{18}_{VSMOW}} - 1, \quad [2]$$

etc.,

$$\Delta^{17}O = \delta^{17}O - 0.516 \times \delta^{18}O, \quad [3]$$

and

$$\Delta_{47} = \left(\frac{R^{47}}{R^{47}_{stoc}} - 1\right) - \left(\frac{R^{46}}{R^{46}_{stoc}} - 1\right) - \left(\frac{R^{45}}{R^{45}_{stoc}} - 1\right), \quad [4]$$

where R^{47} is the mass 47-to-mass 44 ratio of CO_2 and R^{47}_{stoc} is the same ratio if the O and C isotopes are distributed stochastically (44). Only the dominant isotopologues, $^{12}C^{16}O_2$, $^{13}C^{16}O_2$, $^{12}C^{18}O^{16}O$, and $^{13}C^{18}O^{16}O$, were considered when calculating Δ_{47}.

ACKNOWLEDGMENTS. We thank the Initial Training Network in Mass Independent Fractionation sponsored by the European Community's Seventh Framework Program (FP7/2007-2013) under Grant Agreement 237890 and the Gesellschaft für wissenschaftliche Datenverarbeitung mbH Göttingen.

1. Yung YL, DeMore WB (1999) *Photochemistry of Planetary Atmospheres* (Oxford Univ Press, New York).
2. Driese SG, et al. (2011) Neoarchean paleoweathering of tonalite and metabasalt: Implications for reconstructions of 2.69 Ga early terrestrial ecosystems and paleoatmospheric chemistry. *Precambrian Res* 189(1–2):1–17.
3. Bao H, Lyons JR, Zhou C (2008) Triple oxygen isotope evidence for elevated CO_2 levels after a Neoproterozoic glaciation. *Nature* 453(7194):504–506.
4. Clerbaux C, et al. (2005) Carbon monoxide distribution from the ACE-FTS solar occultation measurements. *Geophys Res Lett* 32(16):L16S01.
5. Thiemens MH (1999) Mass-independent isotope effects in planetary atmospheres and the early solar system. *Science* 283(5400):341–345.
6. McGlynn SP, Rabalais JW, McDonald JR, Scherr VM (1971) Electronic spectroscopy of isoelectronic molecules. II. Linear triatomic groupings containing sixteen valence electrons. *Chem Rev* 71(1):73–108.
7. Knowles PJ, Rosmus P, Werner H-J (1988) On the assignment of the electronically excited singlet states in linear CO_2. *Chem Phys Lett* 146(3–4):230–235.
8. Spielfiedel A, et al. (1992) Bent valence excited states of CO_2. *J Chem Phys* 97(11): 8382–8388.
9. Spielfiedel A, Feautrier N, Chambaud G, Rosmus P, Werner H-J (1993) The first dipole-allowed electronic transition $1^1\Sigma_u^+ - X^1\Sigma_g^+$ of CO_2. *Chem Phys Lett* 216(1–2):162–166.
10. Grebenshchikov SY (2012) Communication: Multistate quantum dynamics of photodissociation of carbon dioxide between 120 nm and 160 nm. *J Chem Phys* 137(2): 021101.
11. Schmidt JA, Johnson MS, McBane GC, Schinke R (2012) Communication: Multi-state analysis of the OCS ultraviolet absorption including vibrational structure. *J Chem Phys* 136(13):131101.
12. Schmidt JA, Johnson MS, McBane GC, Schinke R (2012) The ultraviolet spectrum of OCS from first principles: Electronic transitions, vibrational structure and temperature dependence. *J Chem Phys* 137(5):054313.
13. Schinke R (2011) Photodissociation of N2O: Potential energy surfaces and absorption spectrum. *J Chem Phys* 134(6):064313.
14. Schmidt JA, Johnson MS, Schinke R (2011) Isotope effects in N_2O photolysis from first principles. *Atmos Chem Phys* 11:8965–8975.
15. Schmidt JA, Johnson MS, Lorenz U, McBane GC, Schinke R (2011) Photodissociation of N_2O: Energy partitioning. *J Chem Phys* 135(2):024311.
16. Schinke R, Schmidt JA, Johnson MS (2011) Photodissociation of N_2O: Triplet states and triplet channel. *J Chem Phys* 135(19):194303.
17. Hattori S, et al. (2011) Ultraviolet absorption cross sections of carbonyl sulfide isotopologues $OC^{32}S$, $OC^{33}S$, $OC^{34}S$, and $O^{13}CS$: Isotopic fractionation in photolysis and atmospheric implications. *Atmos Chem Phys* 11:10293–10303.
18. Schmidt JA, et al. (2013) OCS photolytic isotope effects from first principles: Sulfur and carbon isotopes, temperature dependence and implications for the stratosphere. *Atmos Chem Phys* 13:511–1520.
19. von Hessberg P, et al. (2004) Ultra-violet absorption cross sections of isotopically substituted nitrous oxide species: $^{14}N^{14}NO$, $^{15}N^{14}NO$, $^{14}N^{15}NO$ and $^{15}N^{15}NO$. *Atmos Chem Phys* 4:1237–1253.
20. Schinke R (1993) *Photodissociation Dynamics, Cambridge Monographs on Atomic, Molecular, and Chemical Physics* (Cambridge Univ Press, Cambridge, UK).
21. Werner H-J, Knowles PJ (1988) An efficient internally contracted multiconfiguration reference configuration interaction method. *J Chem Phys* 89(9):5803–5814.
22. Knowles PJ, Werner H-J (1988) An efficient method for the evaluation of coupling coefficients in configuration interaction calculations. *Chem Phys Lett* 145(6):514–522.
23. Grebenshchikov SY, Raffaele B (2012) Crossing electronic states in the Franck Condon zone of carbon dioxide: A five-fold closed seam of conical and glancing intersections. *J Phys Chem Lett* 3(21):3223–3227.
24. Yoshino K, et al. (1996) Absorption cross section measurements of carbon dioxide in the wavelength region 118.7-175.5 nm and the temperature dependence. *J Quant Spectrosc Radiat Transf* 55(1):53–60.
25. Parkinson WH, Rufus J, Yoshino K (2003) Absolute absorption cross section measurements of CO_2 in the wavelength region 163-200 nm and the temperature dependence. *Chem Phys* 290(2–3):251–256.
26. Karaiskou A, Vallance C, Papadakis V, Vardavas IM, Rakitzis TP (2004) Absolute absorption cross-section measurements of CO_2 in the ultraviolet from 200 to 206 nm at 295 and 373 K. *Chem Phys Lett* 400(1–3):30–34.
27. Stolow A, Lee YT (1993) Photodissociation dynamics of CO_2 at 157.6 nm by photofragment-translational spectroscopy. *J Chem Phys* 98(3):2066–2076.
28. Miller RL, Kable SH, Houston PL, Burak I (1992) Product distributions in the 157 nm photodissociation of CO_2. *J Chem Phys* 96(1):332–338.
29. Chen Z, Liu F, Jiang B, Yang X, Parker DH (2010) Imaging CO_2 photodissociation at 157 nm: State-to-state correlations between $CO(v)$ and $O(^3P_{j=0,1,2})$. *J Phys Chem Lett* 1(12): 1861–1865.
30. Yung YL, Miller CE (1997) Isotopic fractionation of stratospheric nitrous oxide. *Science* 278(5344):1778–1780.
31. Liang M-C, Blake GA, Yung YL (2008) Seasonal cycle of $C^{16}O^{16}O$, $C^{16}O^{17}O$, and $C^{16}O^{18}O$ in the middle atmosphere: Implications for mesospheric dynamics and biogeochemical sources and sinks of CO_2. *J Geophys Res* 113:D12305.
32. Bhattacharya SK, Savarino J, Thiemens MH (2000) A new class of oxygen isotopic fractionation in photodissociation of carbon dioxide: Potential implications for atmospheres of Mars and Earth. *Geophys Res Lett* 27(10):1459–1462.
33. Mahata S, Bhattacharya SK (2009) Anomalous enrichment of ^{17}O and ^{13}C in photodissociation products of CO_2: Possible role of nuclear spin. *J Chem Phys* 130(23): 234312.
34. Mahata S, Bhattacharya SK (2009) Temperature dependence of isotopic fractionation in CO_2 photolysis. *Chem Phys Lett* 477(1–3):52–56.
35. DeMore WB, Mosesman M (1971) Photolysis of CO_2 at 1849 Å. *Journal of the Atmospheric Sciences* 28(6):842–846.
36. Danielache SO, et al. (2012) Photoabsorption cross-section measurements of ^{32}S, ^{33}S, ^{34}S and ^{36}S sulfur dioxide for the $B^1B^1 - X^1A^1$ absorption band. *J Geophys Res* 117: D24301.
37. Hattori S, et al. (2013) SO_2 photoexcitation mechanism links mass-independent sulfur isotopic fractionation in cryospheric sulfate to climate impacting volcanism. *Proc Natl Acad Sci USA* 110:17656–17661.
38. Dunning TH, Jr. (1989) Gaussian basis sets for use in correlated molecular calculations. I. The atoms boron through neon and hydrogen. *J Chem Phys* 90(2):1007–1023.
39. Balint-Kurti GG (2004) Wavepacket theory of photodissociation and reactive scattering. *Advances in Chemical Physics* 128:249–301.
40. Tal-Ezer H, Kosloff R (1984) An accurate and efficient scheme for propagating the time dependent Schrödinger equation. *J Chem Phys* 81(9):3967–3971.
41. Le Quéré F, Leforestier C (1990) Quantum exact three-dimensional study of the photodissociation of the ozone molecule. *J Chem Phys* 92(1):247.
42. Kosloff D, Kosloff R (1983) A Fourier method solution for the time dependent Schrödinger equation as a tool in molecular dynamics. *J Comput Phys* 52(1):35.
43. Schmidt B, Lorenz U 2009 Wavepacket 4.6: A program package for quantum-mechanical wave packet propagation and time-dependent spectroscopy. Available at http://wavepacket.sourceforge.net. Accessed June 6, 2013.
44. Eiler JM (2007) Clumped-isotope geochemistry—The study of naturally occurring, multiply substituted isotopologues. *Earth Planet Sci Lett* 262(3–4):309–327.